Article

Automated Image Segmentation of the Corneal Endothelium in Patients With Fuchs Dystrophy

Palanahalli S. Shilpashree[1], Kaggere V. Suresh[1], Rachapalle Reddi Sudhir[2], and Sangly P. Srinivas[3]

[1] Department of Electronics and Communication Engineering, Siddaganga Institute of Technology (Affiliated to Visvesvaraya Technological University, Belagavi), Tumkur, India
[2] Department of Cornea and Refractive Surgery, Sankara Nethralaya, Chennai, India
[3] School of Optometry, Indiana University, Bloomington, IN, USA

Correspondence: Sangly P. Srinivas, School of Optometry, 800 East Atwater Avenue, Indiana University, Bloomington 47405, USA. e-mail: srinivas@indiana.edu

Purpose: To perform segmentation of specular microscopy (SM) images of the corneal endothelium for comparing average perimeter length (APL) between Fuchs endothelial corneal dystrophy (FECD) patients and healthy subjects.

Methods: A retrospective review of clinical records of FECD patients and those with healthy endothelium was carried out to collect images of the endothelium. The images were segmented by modified U-Net, a deep learning architecture, followed by the Watershed algorithm to resolve merged cell borders (<5%). The segmented images were analyzed for endothelial cell density (ECD_{UW}) and APL.

Results: The combination of the U-Net and Watershed algorithm, referred to as the UW approach, enabled a complete segmentation of the endothelium. In healthy, ECD_{UW} was close to estimates by SM and manual segmentation (31 subjects; $P > 0.1$). However, in FECD, ECD_{UW} was closer to estimates by manual segmentation but not by SM (27 patients; $P < 0.001$). ECD_{UW} in FECD (2547 ± 499 cells/mm^2; 60 patients) was smaller compared to that in the healthy (2713 ± 401 cells/mm^2; 70 subjects) ($P < 0.001$). APL in the healthy was 66.87 ± 7.68 µm/cell (70 subjects), but it increased with %Guttae in FECD (56.60–195.30 µm/cell; 60 patients) ($P < 0.0001$).

Conclusions: The UW approach is precise for the segmentation of SM images from the healthy and FECD. Our analysis has revealed that APL increases with %Guttae.

Translational Relevance: The average perimeter length of the corneal endothelium, which represents the length of the paracellular pathway for fluid flux into the stroma, is increased in Fuchs dystrophy.

Introduction

The corneal endothelium, which forms the posterior monolayer of the cornea, is the guardian of corneal transparency. A state of dehydration of the corneal stroma (i.e., stromal deturgescence), a prerequisite for corneal transparency, is maintained by the endothelium through its barrier and pump functions.[1,2] The barrier function restrains the rate of fluid influx into the stroma from the aqueous humor. The influx arises because of the imbibition pressure induced by the hydrophilic glycosaminoglycans dispersed around the collagen fibrils. The fluid leaking into the stroma, despite the barrier function, is countered by the pump function of the endothelium.[3] Mechanistically, the tight junctions of the endothelium confer the barrier function, and, hence, the junctional length is a determinant of endothelial barrier function. Although the regulation of tight junctions has been investigated,[1,2] variation in its length is not fully understood. In this study, we have determined whether the average perimeter length (APL; i.e., junctional length per cell) of the endothelium is altered in Fuchs endothelial corneal dystrophy (FECD).

Potential for changes in APL during health and FECD exists because of known differences in endothelial cell density (ECD).[4–7] The rate of decline in ECD,

however, is significantly accelerated during FECD.[5,7] The decrease is also rapid following transplantation and intraocular surgeries.[6,7] Since the endothelium in humans is non-regenerative, the denuded Descemet's membrane is re-surfaced by the spreading of neighboring cells. In this process, endothelial cells lose their native hexagonal shape and size.[8,9] Thus unlike in the young and healthy, the endothelial cells show polymegathism (i.e., variable cell size) and pleomorphism (i.e., irregular cell shape) in the elderly. These morphological adjustments inevitably affect the APL. Rannou et al.[10] reported an increase in APL with age. Because the fluid influx through the paracellular space is directly proportional to APL, an increase in the latter has the potential to induce stromal edema if not duly compensated by an intrinsic activation of the fluid pump activity.

For investigating APL, automatic segmentation of the endothelium is an essential first step. In addition, segmentation is also critical for evaluating the donor endothelium before transplantation. Transplantation of donor endothelium with ECD > 2000 cells/mm^2 is the norm for endothelial keratoplasty, which in and of itself leads to significant cell loss because of mechanical trauma.[11] Therefore assessing the ECD of the donor endothelium by specular microscopy (SM) is standard practice. Manual segmentation of the SM images, however, is laborious and prone to errors. Thus automated segmentation techniques have been developed to evaluate ECD.[12–19]

Several approaches have been tested for segmenting the endothelium, including machine learning[18] and deep learning algorithms.[14–16,20] The conventional methods, which involve a combination of image processing such as thresholding, Gaussian filtering, skeletonization, and Watershed algorithm,[12,21,22] are sufficient when the images are of high quality. However, images from patients with FECD could be of poor quality due to epithelial defects, stromal scarring, and edema. Therefore machine learning and deep learning techniques have been adopted for accurate and automated endothelial segmentation.[14–16,19,20]

In this study, we have adapted the U-Net model of convolutional neural network to segment SM images of the endothelium. In particular, we have modified the original U-Net model[23] by downsizing the network to reduce the training time. As an additional step, the U-Net output has been processed further using the Watershed algorithm[24] to achieve a complete cell segmentation. Subsequently, the fully segmented images have been used to compute ECD,[19] coefficient of variation of cell area (CV),[19] %Guttae, APL, and equivalent diameter of cells. With healthy and FECD images, our findings show that APL increases with an increase in %Guttae in FECD. Thus, despite the limited data set, we offer a new window to further understand the pathophysiology of FECD.

Materials and Methods

Data Collection

We performed a retrospective study of patients at the Cornea Clinic of Sankara Nethralaya (Chennai, India). We focused on patients with a record of endothelial images acquired by SM (Tomey EM-3000; Nagoya, Japan). The study protocol adhered to the tenets of the Declaration of Helsinki and was approved by the institutional review board at our eye hospital (Medical Research Foundation, Chennai, India). The FECD cohort consisted of 60 patients (121 images) diagnosed with FECD; they showed guttae in their SM images. We also collected 70 SM images (125 images) without guttae or other anomalies as the healthy cohort. We deidentified the subject/patient information for both cohorts and collected endothelial images, patient demographics, diagnosis, treatment strategies, and other corneal health remarks. The SM images were in bitmap image file (BMP) format with dimensions 266 × 480 and a grey level resolution of eight bits. The images showed variable levels of noise, blur, and contrast, making the segmentation challenging. However, the built-in software of EM-3000 carried out segmentation and provided estimates of ECD and CV.

The primary dataset contained ~300 SM images inclusive of the healthy and FECD images. It was divided into training and testing datasets. A total of 40 images of the healthy and FECD were assigned exclusively as the initial training dataset, which was increased to 2000 images by augmentation (described below). The testing dataset contained 125 healthy images (70 subjects) and 121 FECD images (60 patients). Thus none of the images belonging to the training dataset were used as part of the testing dataset.

Data Augmentation

Because a large number of images and ground truths are required for training the modified U-Net, a data augmentation[25] step on both images and corresponding ground truths has been included. The ground truths, corresponding to the SM images, were generated by drawing with a digital pen. They contained three classes: class 0 for the cell body, class 1 for guttae, and class 2 for cell borders. We used Albumentations, an open-source Python library, for generating the augmented images. In particular, our training dataset

initially contained 40 images and corresponding masks from the healthy and FECD cohorts. The images and related masks were expanded using the Albumentation pipeline, which consisted of horizontal flip, vertical flip, random cropping, random brightness contrast, blur, CLAHE (contrast limited adaptive histogram equalization), and grid distortion.[25] Thus 2000 augmented images and masks were developed and used in turn as the training set.

Network Architecture and Training

We have used the U-Net architecture as described by Ronneberger et al.[23] with a few modifications to reduce the time for training. As shown in Figure 1, U-Net is an encoder-decoder type architecture with the encoder gradually downsizing the spatial dimension of the input data whereas the decoder retrieves the dimensions gradually. The modifications are as follows: we have downscaled the number of layers by eliminating one level of max-pooling/upsampling functions and corresponding convolutional layers. In addition, the

convolutional layers in the first level now consist of 16 feature maps (instead of 64) and were doubled at each max-pooling step, that is, 16, 32, 64, and 128 feature maps along the encoder path. Hence, feature maps varied from 16 to 128 along the encoder path instead of 64 to 1024. Similarly, the feature maps were halved in every upsampling step of the decoder path (i.e., 128, 64, 32, and 16, respectively). Thus there is a notable reduction in feature maps at every step compared to the original U-Net, significantly reducing the time required to train the model.

To summarize, the original U-Net possessed 1941.10×10^3 trainable parameters, whereas the modified U-Net uses only 482.03×10^3. Hence, much less time was required for training our modified U-Net. Finally, we have introduced dropouts at the third and fourth levels of the modified U-Net to reduce overfitting. The modified U-Net is illustrated in Figure 1, highlighting the contraction and expansion paths. Each step along the contraction path consisted of two 3×3 padded convolutions followed by Rectified Linear Activation function.[26] This is accompanied by a 2×2 max-pooling operation with a stride of 2 pixels
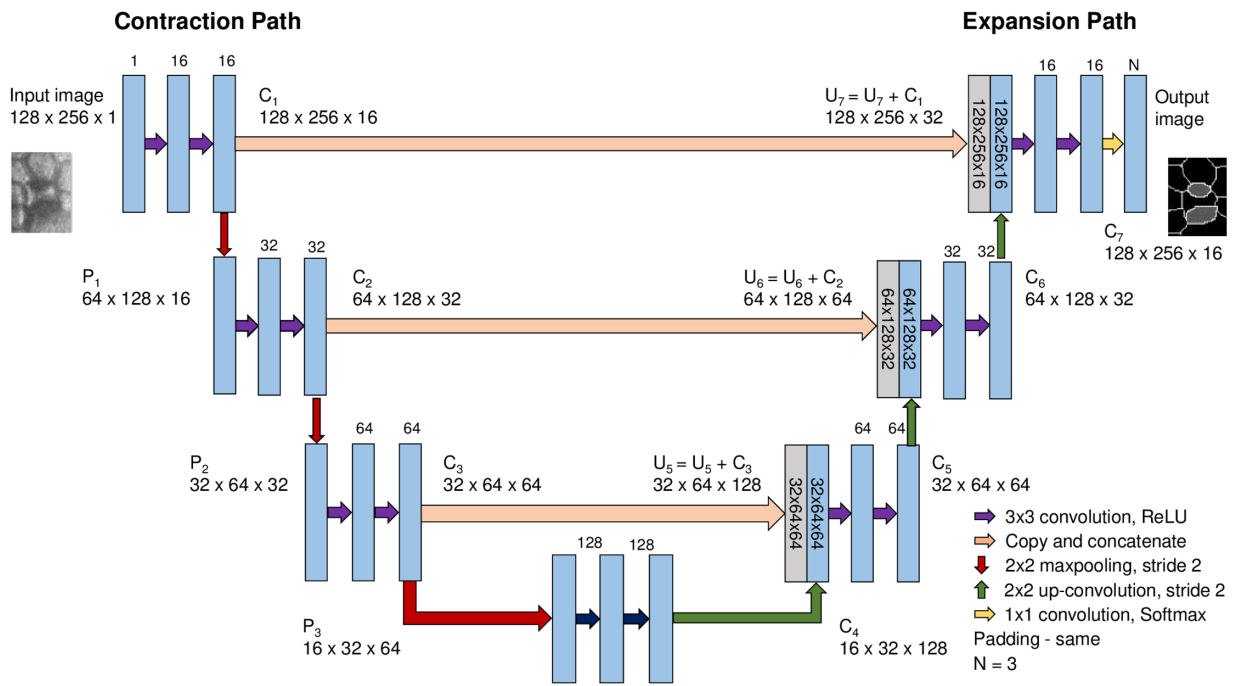
Figure 1. Modified U-Net architecture for multiclass image segmentation. The contraction path (i.e., encoder path) is shown on the left side, where regular convolutions and max-pooling layers are applied. Down the encoder, the size of the image reduces, but feature maps increase gradually. The expansion path (i.e., decoder path) is shown on the right-hand side, where transposed convolutions along with regular convolutions are applied. Up the decoder, the image size gradually increases, but the feature maps decrease. At every step of the decoder, we use skip connections by concatenating the output of the transposed convolution layers with the feature maps from the encoder at the same level: i.e., $U_5 = U_5 + C_3$, $U_6 = U_6 + C_2$, and $U_7 = U_7 + C_1$. Two consecutive regular convolutions are applied after every concatenation. The number of features is denoted on top of the blue box. *Gray boxes* represent copied feature maps. C_1–C_7 are the output tensors of the convolutional layers. P_1–P_3 represent the output tensors of the max-pooling layers; U_5–U_7 are the output tensors of the up-sampling (transposed convolutional) layers.

for downscaling. The feature maps are doubled at every downsampling step. As a result, the input image size reduces from 128×256 to 16×32 in the encoder path. The operations performed at the expansion path are similar to that of the contraction path, except for the upsampling operation with a factor of 2 instead of max pooling. Upsampling was performed using 3×3 transposed convolutions with a stride of 2 pixels. As a result, the input image size increases from 16×32 to 128×256 in the expansion path. The numbers of convolutional layers, feature maps, and dropouts of the network were selected via experimentation with the clinical data. The Adam optimizer and the categorical cross-entropy loss function (with Softmax activation function) were used in the last convolutional layer, generating three probability maps, one for cell body, one for guttae, and the other for cell border.

The modified U-Net was trained for 60 epochs with a batch size of 8 using 2000 augmented images and corresponding masks/ground truths of dimension 128×256. The Adam optimizer employed in training the model minimized the loss function. The model was built with Python 3.7 using the Keras library and Tensorflow backend. We trained the modified U-Net on a GeForce GTX-1080 TI GPU with 32 GB of RAM.

Watershed Algorithm

In the initial trials, the segmentation by the modified U-Net was incomplete for poor-quality images. Specifically, for some cells, the boundaries were merged ($\sim$5%). Therefore we post-processed such merged boundaries by applying the Watershed algorithm's marker-based classic image segmentation technique.[24] The entire postprocessing step was automated using OpenCV in Python.

Traditional image processing methods, such as thresholding and contour detection, fail to extract overlapping objects in images. As a classic algorithm, the Watershed algorithm is beneficial for extracting merged and overlapping objects in images. To obtain an accurate segmentation, the markers were placed on individual cells. First, a distance map was obtained by applying Euclidean distance transform, and local maxima were computed. Then markers were placed automatically using connected component analysis. Thus our process of endothelial segmentation is fully automated.

Performance Metrics

To underscore the performance of the modified U-Net algorithm, we calculated the F1 score, mean

IoU, and pixel accuracy.[27] The F1 score (also known as Dice Coefficient) is calculated as twice the area of overlap between ground truth (G) and segmentation output (predicted; P) divided by the total area of predicted and the ground truth (Equation 1). IoU (also known as Jaccard Index) is similar to the F1 score and quantifies the %overlap between ground truth (G) and segmentation output (P). In addition, it is calculated by the intersection of the predicted segmentation and the ground truth divided by the union between the predicted segmentation and the ground truth (Equation 2). Finally, pixel accuracy is the % of pixels in the image that is segmented correctly (Equation 3).

$$F1\ score = D\ (P \cap G) = \frac{2\,|P \cap G|}{|P| + |G|} \tag{1}$$

$$IoU = \frac{|P \cap G|}{|P \cup G|} \tag{2}$$

$$Pixel\ accuracy = \frac{TP + TN}{TP + TN + FP + FN} \tag{3}$$

where P is the predicted image and G is the ground truth, TP is true positive, TN is true negative, FP is false positive, and FN is false negative.

Morphometric Analysis

The output of the UW algorithm was further implemented in python using the OpenCV library to carry out a morphometric analysis. In particular, we computed ECD, CV, %Guttae, APL, and equivalent diameter of cells as follows:

$$ECD = \frac{n}{\sum_{i=1}^{n} C_i} \tag{4}$$

$$CV = \frac{1}{\bar{C}} \sqrt{\frac{1}{n} \sum_{i=1}^{n} \left(C_i - \bar{C}\right)^2} \tag{5}$$

$$\%Guttae = \frac{\sum_{j=1}^{k} G_j}{\sum_{i=1}^{n} C_i + \sum_{j=1}^{k} G_j} \tag{6}$$

$$APL = \frac{\sum_{i=1}^{n} P_i}{n} \tag{7}$$

$$ED_{Cell} = 2 \sqrt{\frac{C_i}{\pi}} \tag{8}$$

where C_i is the area of the ith cell, G_j indicates the area of the jth guttae, P_i represents perimeter length

of the ith cell, n represents the number of endothelial cells, k stands for the number of guttae, and $\bar{C}$ denotes average cell size. We note that ECD (cells/mm^2) and APL (µm/cell) are based on the number of cells and cell area (i.e., guttae area are excluded). Therefore %Guttae can be taken as an approximate measure of severity of FECD. In general, an increase in guttae and their coalescence are noticed in advancing FECD.[4–7] However, we note that our calculations are based on limited endothelial images from the affected cornea.

Results

Our retrospective review of medical records led to a collection of data on 60 FECD patients (age 48.76 ± 20.12 years, interquartile range [IQR]: 27–65 years; 17 males and 43 females) and 70 healthy subjects (Age: 49.55 ± 18.71 years, IQR: 34–64 years; 33 males and 37 females). There was no difference between the mean ages in the two cohorts ($P = 0.8009$). In general, the images were of variable quality, and the number of images was not sufficient for training the model. Therefore we carried out the data augmentation step. Figure 2 shows the augmentation pipeline applied to create a new collection of images and their corresponding ground truths. Overall, our data augmentation step led to 2000 images and corresponding masks, which constituted the dataset for training the modified U-Net.

Automated Segmentation

The modified U-Net model implemented in this study has fewer trainable parameters and, hence, could be trained rapidly (∼2 hours). Following training with augmented images and corresponding masks with and without FECD, we performed segmentation of the SM images and computed the performance metrics using Equations 1 to 3. We found an F1 score of 82.27% and a mean IoU of 77.27%, highlighting the effectiveness of segmentation despite poor-quality images. Accuracy provides the percentage of pixels correctly in the segmented image. Thus it is an alternative metric to evaluate segmentation. We found the accuracy to be 87.9%. Furthermore, the model's performance in recognizing the cell borders is also shown by the receiver operating characteristic (ROC) curve
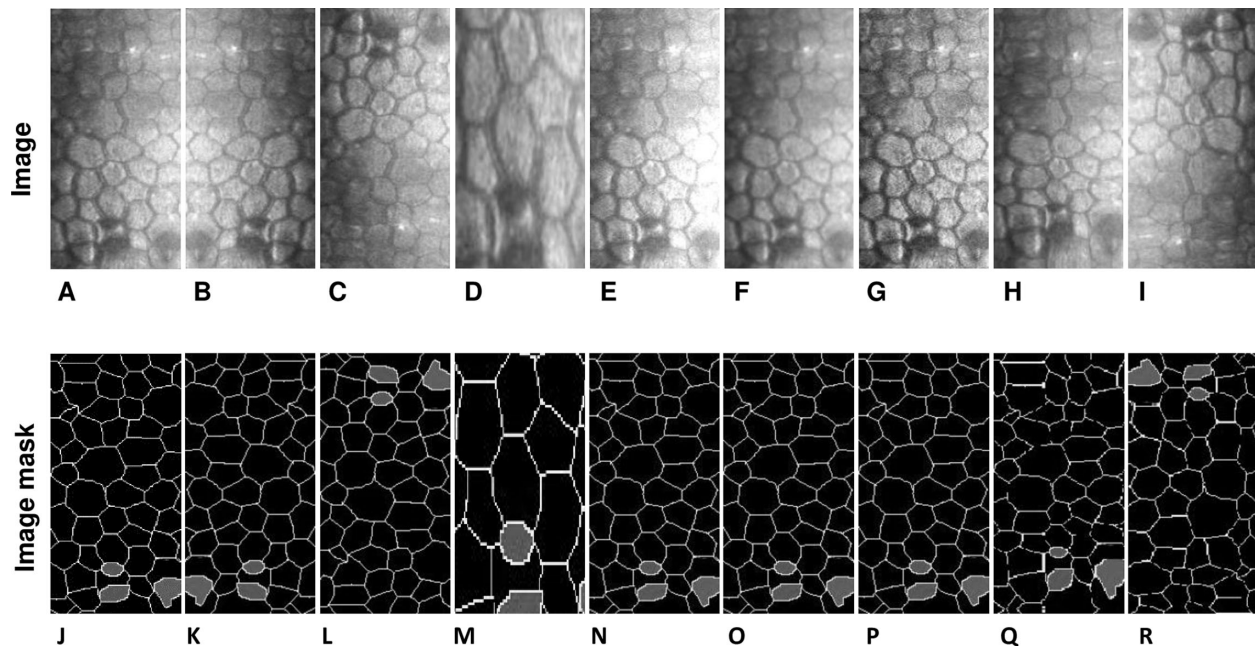
Figure 2. Augmentation of clinical images to generate the training set for modified U-Net. **(A)** The original image of an FECD patient obtained using the noncontact SM. The image in Panel **J** was generated by manual drawing as the ground truth for Image **A**. This ground truth image has class 0 for cell body, class 1 for guttae, and class 2 for cell borders. **(B–H)** Intermediate images obtained by performing horizontal flip, vertical flip, random cropping, random brightness contrast, blur, CLAHE, and grid distortion, respectively, of **A**. Images **B–H** are then pipelined to produce Image **I**, which then forms a member of the training set. Masks **K–Q** represent the ground truths corresponding to Images **B–H**, generated by the augmentation algorithm. The augmentation procedure was repeated to generate multiple images and corresponding masks equivalent to **I** and **R** from every clinical sample, such as **A** and **J**, respectively. Overall, the augmentation procedure enabled a generation of an extensive training set from a limited number of images as required by the modified U-Net.
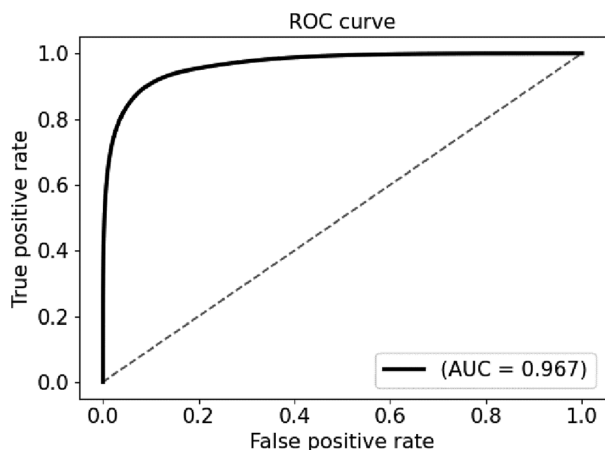
Figure 3. Performance of modified U-Net. The receiver operating characteristics (ROC) curve indicating the performance of U-Net in segmenting the cell body, cell borders, and guttae. The area under the curve (AUC) extracted from the ROC curve is 96.7%, which indicates excellent model performance.

in Figure 3. The area under the ROC curve is 96.7%, indicating a high segmentation quality.

Figure 4 shows typical cell segmentation results of the UW approach for healthy (Panels A–D) and FECD corneas (Panels E–J). In particular, Panel B is the output of the modified U-Net for the SM image in Panel A. Panel C is similar to Panel B, except that cells touching the image borders have been removed automatically. Moreover, arrows in Panel C highlight the cells that U-Net did not resolve. Therefore we processed the modified U-Net output with the Watershed algorithm to segment merged cells, typically < 5% in an image. This combination, referred to as the UW approach, led to complete segmentation (Panel D). A similar workflow for segmentation of an FECD image is depicted in Panels E to J. Figure 5 shows the segmentation of SM images (Panels A–C) by the fully automated UW approach (Panels D–F) and their comparison with images obtained by manual segmentation (Panels G–I).

Morphometric Analysis

Using the output of the UW workflow, we computed ECD (Equation 4), CV (Equation 5), %Guttae (Equation 6), APL (Equation 7), and equivalent diameter of the endothelial cells (Equation 8). The computed ECD and CV values agree with estimates provided by SM and manual segmentation. Figures 6 and 7 provide a Bland-Altman analysis for comparison of ECD estimates by different methods. In healthy subjects, ECD by Tomey's SM software ranged from 1700 to 3400 cells/mm^2 with an IQR of 2627–2932 cells/mm^2 (n = 31 patients, 60 images). As shown

in Figures 6A to 6C, there is an excellent agreement between different ECD estimates. This is confirmed by one-way ANOVA, as shown in Figure 6D ($P > 0.38$ for the different comparisons). Similar to healthy subjects, we report different ECD estimates from FECD patients in Figure 7. ECD varied relatively widely with 600 to 3000 cells/mm^2 with an IQR of 2058 to 2818 cells/mm^2 (n = 27 patients, 52 images), unlike in the healthy subjects. Nonetheless, the ECD estimates of the UW approach, Tomey's SM software, and manual segmentation are not significantly different from each other (Fig. 7D; $P > 0.14$).

The size distributions (based on equivalent diameter) were Gaussian in both the healthy and FECD. The distribution was relatively narrow in the healthy (29.66 ± 6.83 µm; IQR: 25.07–33.55 µm) compared to that in the FECD (29.95 µm ± 9.53 µm; IQR: 23.67–34.81 µm) as shown in Figure 8A. Because ECD declines more rapidly with FECD, polymegathism and pleomorphism would be pronounced during the disease. More importantly, from the perspective of the barrier function of the endothelium, APL increased by ~300% in the FECD (compared to the mean APL in the healthy). It was 66.87 ± 7.68 µm/cell with an IQR: 61.87–70.79 µm/cell in the healthy (n = 70 patients, 125 images) but it was much higher in the FECD (87.87 ± 26.06 µm/cell; IQR: 69.21–101.1 µm/cell, n = 60 patients, 121 images) as shown in Figure 8B ($P < 0.0001$). Figure 9 shows variations in ECD and APL with the severity of FECD. In particular, APL in the FECD increased with %Guttae (Fig. 9A), but the increase is not apparent until %Guttae reaches ~5%. On the other hand, ECD in the FECD appears to decline with %Guttae from early stages (i.e., even before 5% guttae; Fig. 9B).

Discussion

We have modified the original U-Net architecture described by Ronneberger et al.[23] for automated segmentation of corneal endothelial mosaics. We have also added the Watershed algorithm as a postprocessing step to resolve merged cells in the output of the U-Net. The UW approach provided a complete segmentation in both the normal and FECD endothelial mosaics. Following segmentation, we have found that ECD and APL are altered with an increase in %Guttae. The increase in APL, in addition to declining ECD, suggests a potential for an increased burden on the barrier function of the endothelium during FECD.

Despite a significant success with modified U-Net, we observed an incomplete segmentation. Typically
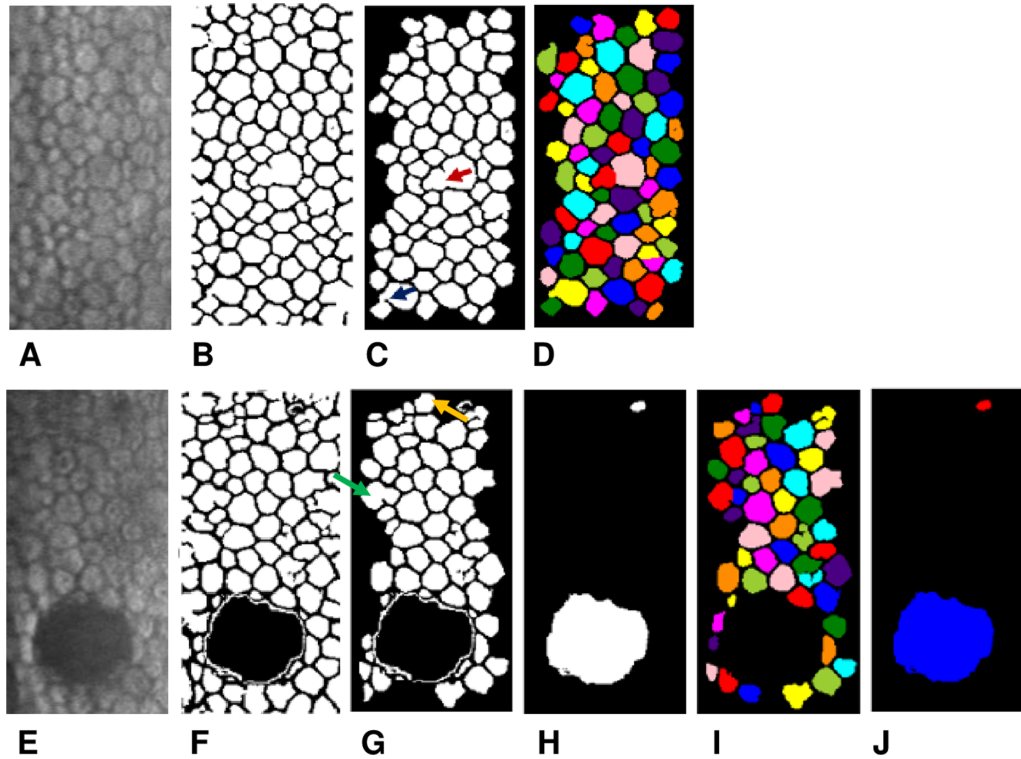
Figure 4. Automated cell segmentation by the UW approach for a healthy subject **(A–D)** and an FECD patient **(E–J)**. **(A)** SM image of a subject with unclear borders. **(B and C)** Output of modified U-Net, where the cells touching the borders are automatically removed in **C**. The *red* and *blue arrows* of **C** show merged cells. **(D)** The output of UW approach, where the Watershed algorithm was applied to the output of the modified U-Net (i.e., the image in **C**). The postprocessing has resolved the borders of all the merged cells. **(E)** SM image of an FECD patient, where guttae can be seen at the bottom of the image. **(F and G)** Output of modified U-Net, which contains only cells (guttae are excluded). Cells touching the borders are automatically removed in **G**. The *yellow* and *green arrows* of **G** show merged cells. **(H)** Output of modified U-Net, with guttae extracted. **(I)** The output of the UW approach, where the Watershed algorithm was applied to the output of the modified U-Net (i.e., the image in **G**). The post-processing has resolved the borders of all the merged cells. **(J)** The output of the UW approach, which was applied to the output of the modified U-Net (i.e., the image in **H**).
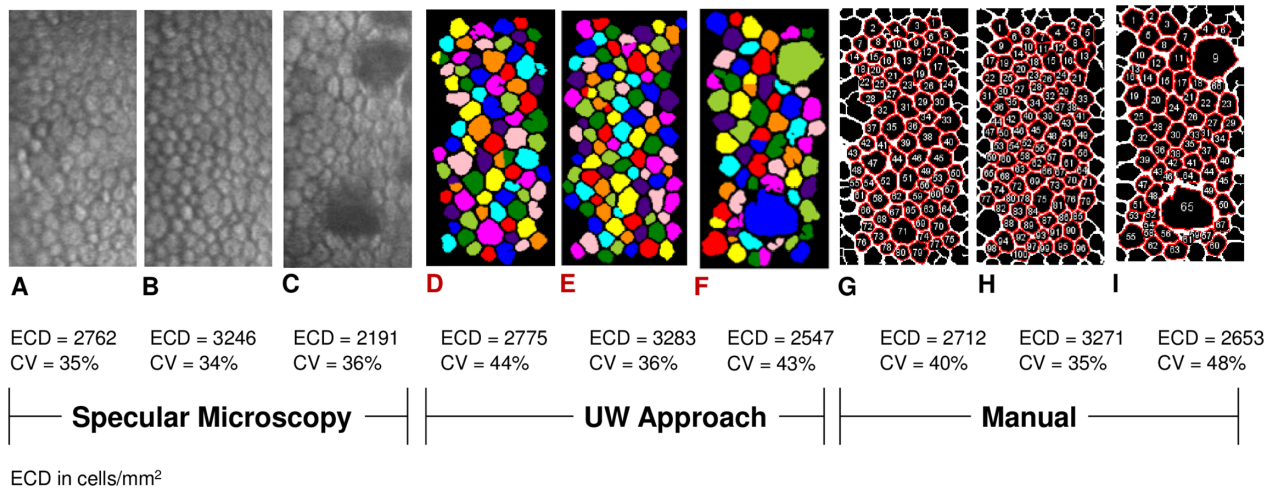
Figure 5. Cell segmentation by the UW approach versus manual segmentation. **A–C** are typical SM images. While **B** and **C** are images from healthy subjects, **C** is an image from an FECD subject. **D–F** are segmented images produced by the UW approach, and they correspond to raw images in **A–C**, respectively. Cells touching the image borders were deselected automatically by the UW approach, and these cells were not considered for the analysis of the morphometric parameters. **G–I** are the ground truth images corresponding to raw images in **A–C**, respectively. ECD and CV computed using segmented images of the UW approach are close to those provided by SM and computed by manual segmentation.
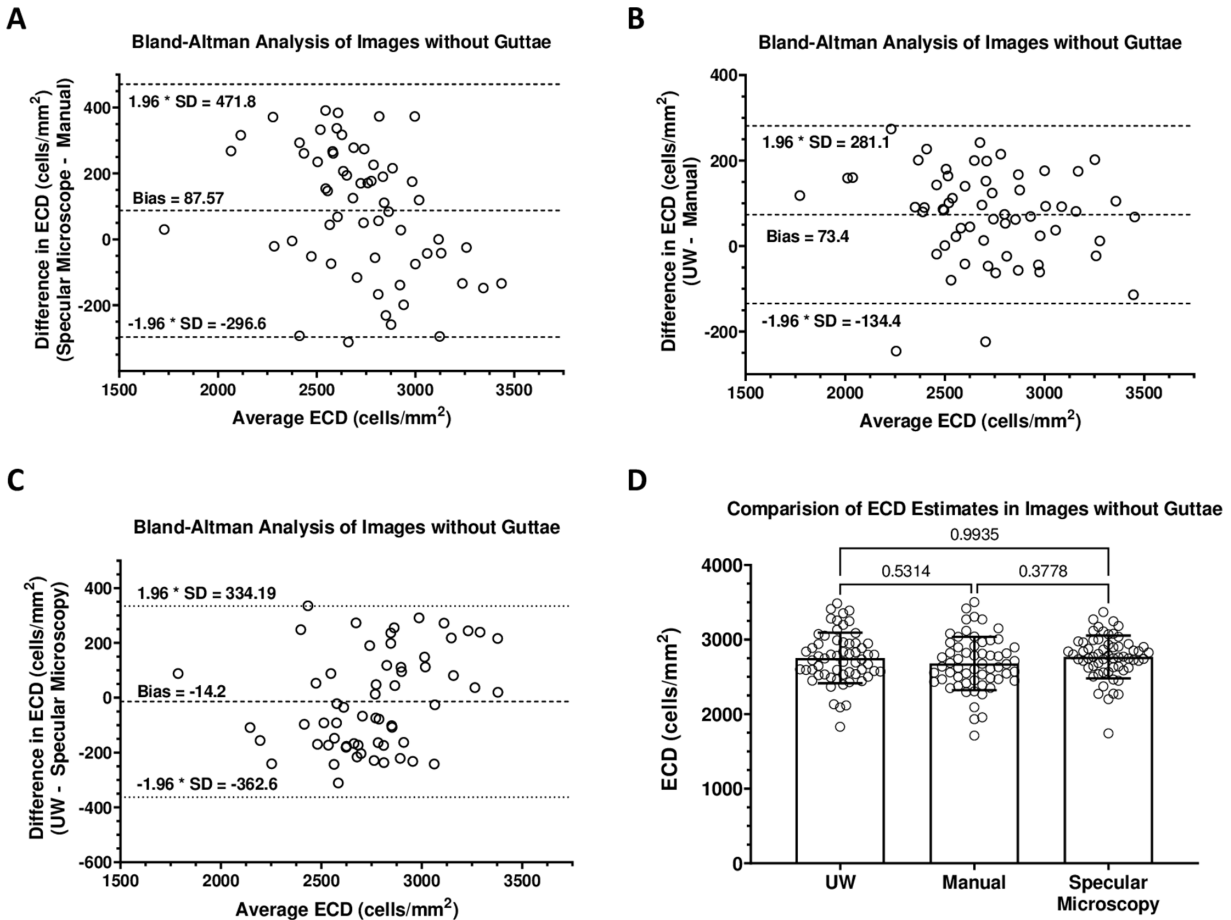
Figure 6. Comparison of ECD estimates for healthy subjects: ECD estimates of 60 images from healthy subjects were compared by the UW approach with that provided by SM and ground truths which were segmented manually. The *middle line* represents the mean difference, and the *dashed lines* show the 95% LoAs. ECD ranged from 1700 to 3500 cells/mm² in all the methods. **(A)** Bland-Altman analysis between the SM and manual segmentation. **(B)** Bland-Altman analysis between UW approach and manual segmentation. **(C)** Bland-Altman analysis between UW approach and SM software. **(D)** Comparison of ECD estimates in all the methods: There is no significant difference between ECD estimates of the three methods ($P > 0.38$).

~5% of cells remained unresolved with merged boundaries in many SM images. To overcome this problem, we processed the U-Net output with the Watershed algorithm, which has been used before as a stand-alone technique for segmenting endothelial images.[24] Thus, unlike other reports on endothelial segmentation,[14,15] the inclusion of the Watershed algorithm for postprocessing was critical to secure an improved accuracy of the segmentation. As a result, the UW approach could be applied successfully even to FECD images, which are corrupted secondary to corneal edema.

To assess the performance of the modified U-Net, we computed different metrics. Thus we found an F1 score of 82.27%, a mean IoU of 77.27%, and an accuracy of 87.9%. In addition, the area under the ROC curve is 96.70%. In agreement with our observations in the healthy subjects, Fabijańska[28] obtained an average F1 score of 83% from images of Alizarine-

red stained endothelium from 30 healthy subjects. In another study, Fabijańska[15] reported an area under the ROC curve as 92% and an F1 score of 86% based on 30 healthy images. Kolluru et al.[29] achieved a mean F1 score of 86% and a mean IoU of 75% with the U-Net approach for a dataset containing 130 images of post-endothelial keratoplasty in a Cornea Preservation Time Study. Using the U-Net, Vigueras-Guillén showed an F1 score of 98% with 50 images from the central cornea of 50 glaucomatous eyes imaged with a Topcon's SM (SP-1P, Topcon Co, Japan).[19] Thus the metrics obtained by our workflow with the modified U-Net and FECD images are relatively close to values reported previously with healthy images.

Apart from the metrics of segmentation, we compared estimates of ECD by the three methods. The differences in ECD estimates between Tomey's
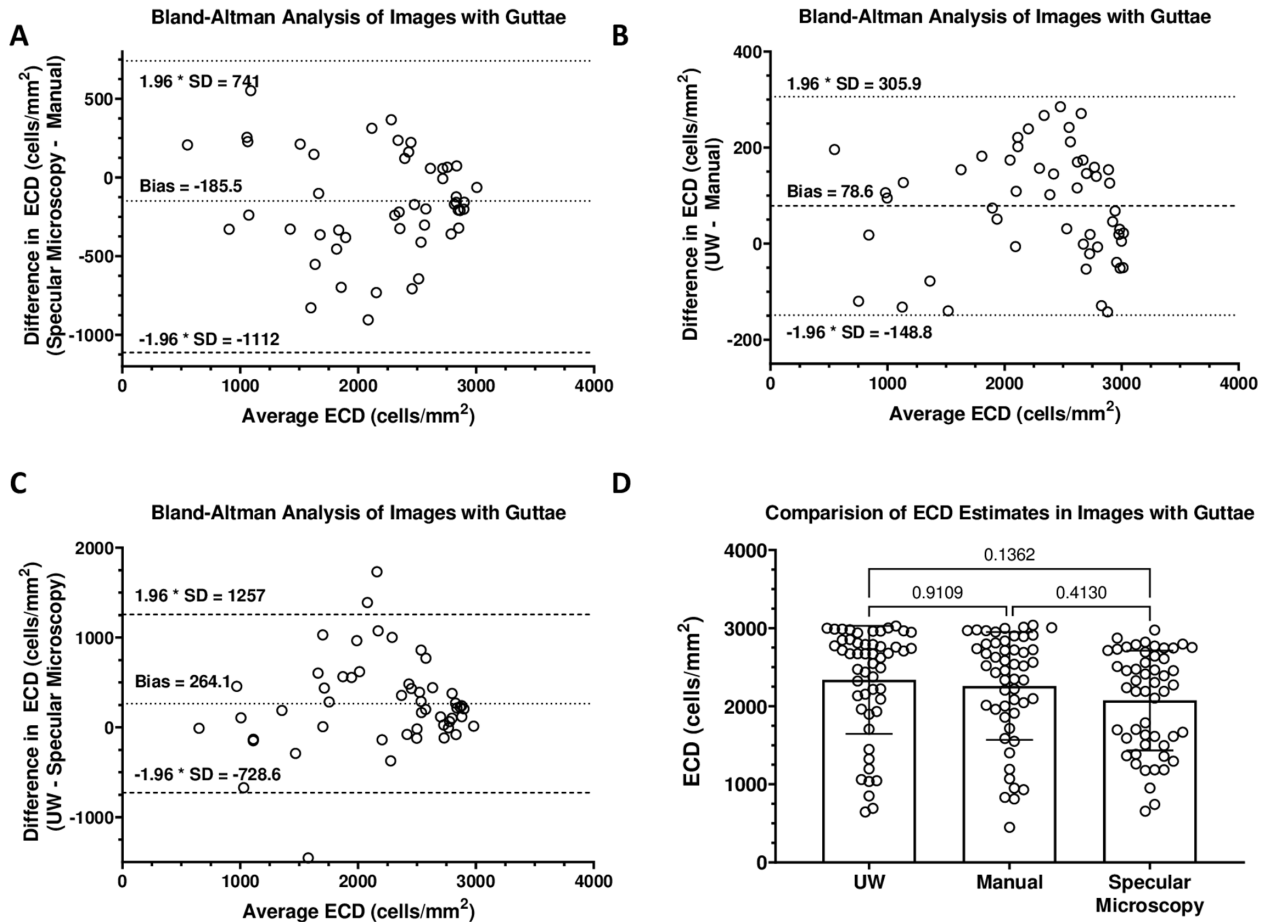
Figure 7. Comparison of ECD estimates for FECD: ECD estimates of 27 subjects (52 images) with FECD by UW approach were compared with that provided by the SM and ground truths, which were segmented manually. The middle line represents the mean difference, and the dashed lines show the 95% LoAs. ECD ranged from 450 to 3000 cells/mm^2 in all the methods. **(A)** Bland-Altman analysis between the SM and manual segmentation. **(B)** Bland-Altman analysis between UW approach and manual segmentation. **(C)** Bland-Altman analysis between UW approach and SM. **(D)** Comparison of ECD estimates of all the methods: There is no significant difference between ECD estimates from the three methods ($P > 0.14$).
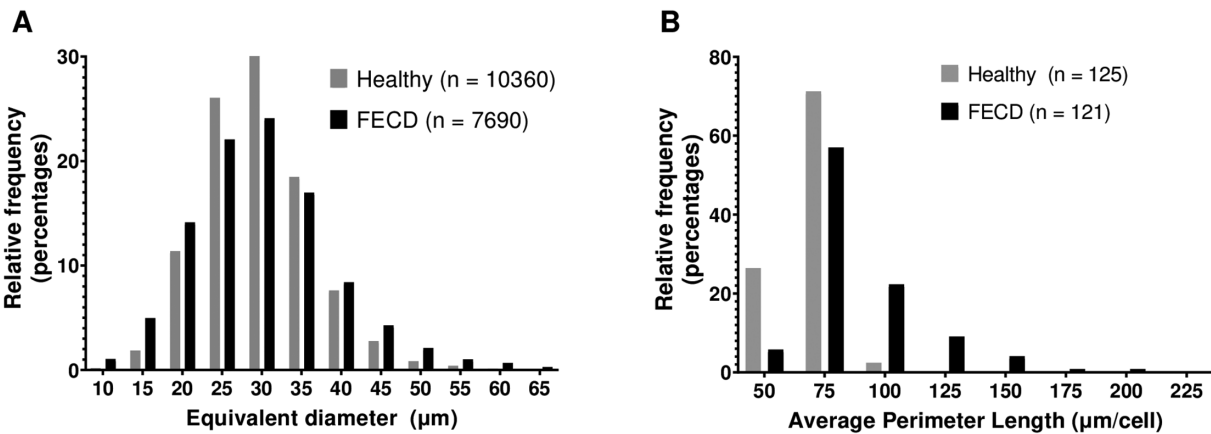
Figure 8. Morphological analysis of the segmented endothelial cells: Histogram of equivalent diameter and APL in the healthy and FECD after segmentation. **(A)** Equivalent diameter: This parameter was calculated based on cell areas assuming a spherical geometry. The distribution of equivalent diameter is Gaussian in the healthy (*gray bars*), with the diameter showing a narrow distribution size (29.66 ± 6.83 µm). The distribution is also Gaussian in FECD (*black bars*) but shows a broader distribution (29.95 µm ± 9.53 µm). **(B)** APL: The distribution is more skewed in FECD compared to healthy. The range of APL in healthy is 53.09 to 94.11 µm/cell compared to 56.6 to 195.3 µm/cell.
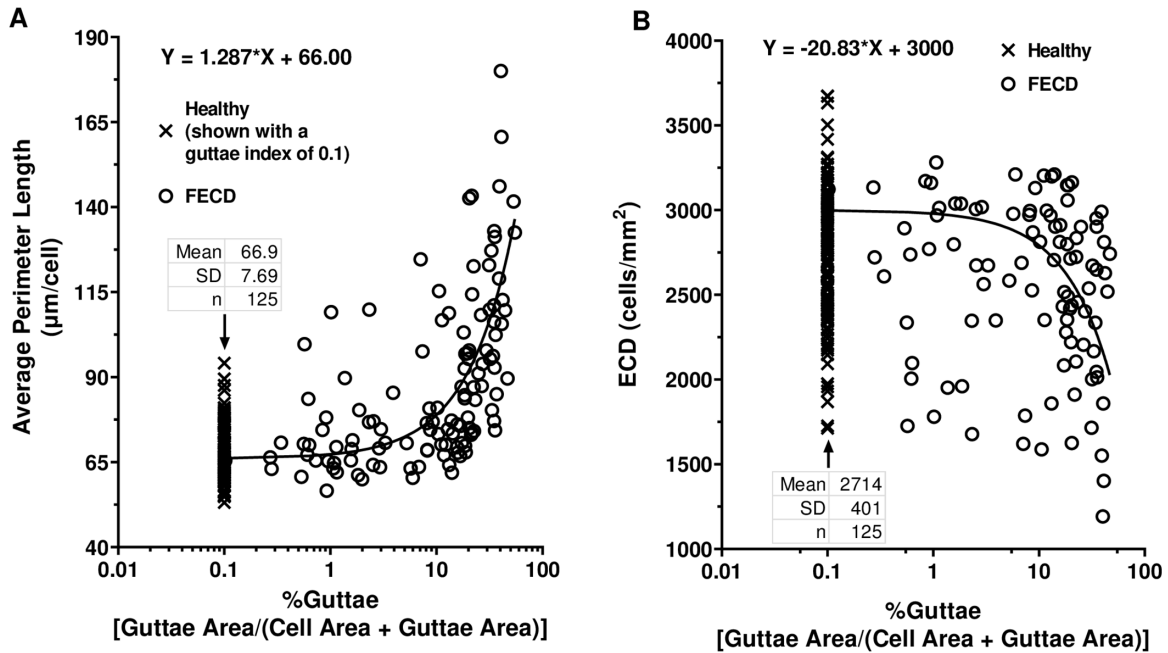
Figure 9. Effect of severity of FECD on the APL and ECD: APL and ECD for healthy subjects and FECD patients computed following segmentation are plotted against %Guttae. **(A)** APL versus %Guttae: APL increased with an increase in severity of guttae (i.e., with an increase in %Guttae). **(B)** ECD versus %Guttae: ECD decreases with an increase in severity of guttae (i.e., with an increase in %Guttae).
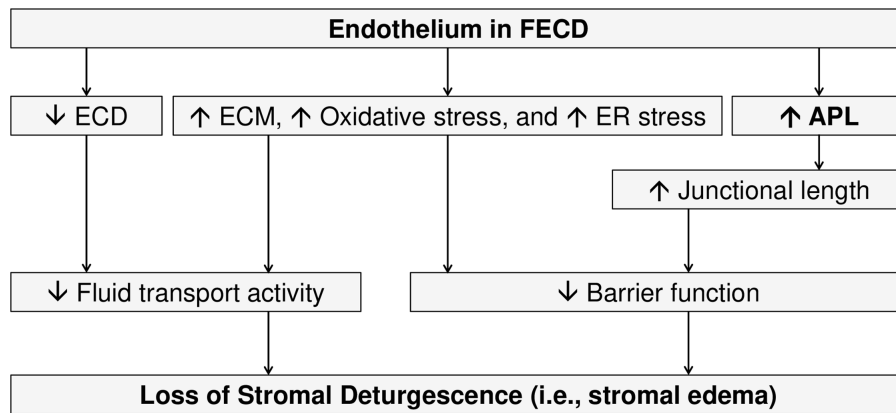
Figure 10. Impact of elongation in APL: The main hallmarks of FECD include a decline in ECD concomitant with increased secretion of extracellular matrix (ECM; which results in guttae), oxidative stress, and endoplasmic reticulum (ER) stress. In this study, we report an increase in APL during FECD. The decline in ECD, which reduces the net fluid transport, is frequently attributed to stromal edema in FECD. In addition, loss of barrier function is reported in FECD, which can be attributed to intracellular stresses and the abnormal ECM. We hypothesize that elongation of APL, which increases the junctional length, also contributes to stromal edema via a reduction in barrier function. Thus studies pertaining to mechanisms that impact the barrier function assume importance in the development of therapeutics of corneal edema in FECD.

SM software versus manual segmentation are minor in healthy (without guttae) compared to FECD. This is indicated by the smaller distance between upper and lower limits of agreement (LoAs) in the healthy compared to FECD (Fig. 6A vs. 7A; 769 cells/mm^2 vs. 1853 cells/mm^2). The trend for the differences in ECD estimates between the UW and SM software remains the same (Fig. 6C vs. 7C; 697 cells/mm^2 vs. 1986 cells/mm^2). In contrast, we note that the differences in ECD estimates between UW and manual are minimal (Fig. 6B vs. 7B; 415 cells/mm^2 vs. 455 cells/mm^2). These observations, however, are not apparent in one-way ANOVA analyses (Figs. 6D and 7D), which indicate a lack of any difference between ECD estimates between

the different methods ($P > 0.37$ for healthy; Fig. 6D and $P = 0.14$ for FECD; Fig. 7D). Overall, assuming the manual segmentation as the gold standard, Bland-Altman's analyses in Figures 6 and 7 suggest that the UW approach agrees very well with the manual segmentation, as highlighted by a small distance between LoAs.

Our morphometric analysis focused on ECD, CV, %Guttae, APL, and equivalent diameter of cells in the healthy *vs.* FECD endothelium. The induction of polymegathism during FECD is evidenced by a large SD in the equivalent diameter (9.53 μm for the FECD *vs.* 6.83 μm for the healthy). This is also confirmed by the skewed distribution of the histogram of equivalent diameter (Fig. 8A). The APL distribution is also significantly skewed in the case of the FECD (Fig. 9B). Although ~58% in both the healthy and FECD cells possess an APL of 75 μm, there are >30% of FECD cells with an APL of >100 μm while >20% of healthy cells possess an APL of 50 μm (Fig. 8B). These dichotomous observations suggest that the overall APL in the FECD is significantly larger than in the healthy. The increase in APL implies an elongation of the paracellular pathway for the inward flux of water from the anterior chamber into the stroma. In other words, there is a propensity for enhanced water leak into the stroma during FECD, potentially leading to stromal edema in the absence of a parallel stimulation in oppositely directed fluid movement. Figure 9A shows that APL elongates as %Guttae increases.

As it is well known from recent studies on FECD,[4–7] the significant hallmarks of the disease include (a) accumulation of abnormal extracellular matrix as guttae, (b) increasing intracellular oxidative stress, and (c) endoplasmic reticulum stress (Fig. 10). Although these mechanisms are implicated in endothelial apoptosis, leading to a decline in ECD, these conditions may also induce intracellular stresses leading to a breakdown of the barrier function.[1,2] Thus the increase in APL during FECD indirectly results in an elongation of the junctional length (Fig. 10). These considerations suggest the importance of rescuing the barrier function in the treatment of stromal edema during FECD.

In conclusion, we have developed the UW algorithm for automatic segmentation of the corneal endothelium. The modified U-Net is versatile because it can be trained rapidly with a smaller training set and produces accurate segmentation. The latter is aided partly by the inclusion of the Watershed algorithm as a postprocessing step to handle unresolved borders in the output of the modified U-Net. Our morphometric analysis has revealed that APL is escalated in FECD, and the increase occurs concomitantly with a decline in ECD.

References

1. Srinivas SP. Dynamic regulation of barrier integrity of the corneal endothelium. *Optom Vis Sci*. 2010;87:E239–E254.
2. Srinivas SP. Cell signaling in regulation of the barrier integrity of the corneal endothelium. *Exp Eye Res*. 2012;95:8–15.
3. Bonanno JA. Identity and regulation of ion transport mechanisms in the corneal endothelium. *Prog Retin Eye Res*. 2003;22:69–94.
4. Jurkunas UV. Fuchs Endothelial Corneal Dystrophy Through the Prism of Oxidative Stress. *Cornea*. 2018;37(Suppl 1):S50–S54.
5. Nanda GG, Alone DP. REVIEW: Current understanding of the pathogenesis of Fuchs' endothelial corneal dystrophy. *Mol Vis*. 2019;25:295–310.
6. Ong Tone S, Kocaba V, Bohm M, Wylegala A, White TL, Jurkunas UV. Fuchs endothelial corneal dystrophy: The vicious cycle of Fuchs pathogenesis. *Prog Retin Eye Res*. 2021;2020100863.
7. Zhang J, McGhee CNJ, Patel DV. The Molecular Basis of Fuchs' Endothelial Corneal Dystrophy. *Mol Diagn Ther*. 2019;23:97–112.
8. Doughty MJ. Concerning the symmetry of the 'hexagonal' cells of the corneal endothelium. *Exp Eye Res*. 1992;55:145–154.
9. Doughty MJ. The ambiguous coefficient of variation: Polymegethism of the corneal endothelium and central corneal thickness. *Int Contact Lens Clinic*. 1990;17:240–248.
10. Rannou K, Crouzet E, Ronin C, et al. Comparison of corneal endothelial mosaic according to the age: the corimmo 3D project. *Irbm*. 2016;37:124–130.
11. Gain P, Jullienne R, He Z, et al. Global Survey of Corneal Transplantation and Eye Banking. *JAMA Ophthalmol*. 2016;134:167–173.
12. Bullet J, Gaujoux T, Borderie V, Bloch I, Laroche L. A reproducible automated segmentation algorithm for corneal epithelium cell images from in vivo laser scanning confocal microscopy. *Acta Ophthalmol*. 2014;92:e312–e316.
13. Selig B, Vermeer KA, Rieger B, Hillenaar T, Hendriks CLL. Fully automatic evaluation of

the corneal endothelium from in vivo confocal microscopy. *BMC Med Imaging*. 2015;15:1–15.

14. Daniel MC, Atzrodt L, Bucher F, et al. Automated segmentation of the corneal endothelium in a large set of "real-world" specular microscopy images using the U-Net architecture. *Sci Rep*. 2019;9:1–7.

15. Fabijańska A. Segmentation of corneal endothelium images using a U-Net-based convolutional neural network. *Artif Intell Med*. 2018;88:1–13.

16. Joseph N, Kolluru C, Benetz BA, Menegay HJ, Lass JH, Wilson DL. Quantitative and qualitative evaluation of deep learning automatic segmentations of corneal endothelial cell images of reduced image quality obtained following cornea transplant. *J Med Imaging*. 2020;7:014503.

17. Scarpa F, Ruggeri A. Segmentation of corneal endothelial cells contour by means of a genetic algorithm. *Ophthalmic Medical Image Analysis International Workshop* 2015:25–32.

18. Vigueras-Guillén JP, Andrinopoulou E-R, Engel A, et al. Corneal endothelial cell segmentation by classifier-driven merging of oversegmented images. *IEEE Trans Med Imaging*. 2018;37:2278–2289.

19. Vigueras-Guillén JP, Sari B, Goes SF, et al. Fully convolutional architecture vs sliding-window CNN for corneal endothelium cell segmentation. *BMC Biomed Eng*. 2019;1:1–16.

20. Vigueras-Guillén JP, van Rooij J, Engel A, Lemij HG, van Vliet LJ, Vermeer KA. Deep learning for assessing the corneal endothelium from specular microscopy images up to 1 year after ultrathin-DSAEK surgery. *Transl Vis Sci Technol*. 2020;9:49–49.

21. Sanchez-Marin FJ. Automatic segmentation of contours of corneal cells. *Comput Biol Med*. 1999;29:243–258.

22. Gavet Y, Pinoli J-C. Visual perception based automatic recognition of cell mosaics in human corneal endothelium microscopy images. *Image Analysis Stereol*. 2008;27:53–61.

23. Ronneberger O, Fischer P, Brox T. *U-Net: Convolutional Networks for Biomedical Image Segmentation*. In: Navab N., et al., eds. Cham: Springer International Publishing; 2015:234–241.

24. Grau V, Mewes A, Alcaniz M, Kikinis R, Warfield SK. Improved watershed transform for medical image segmentation using prior information. *IEEE Trans Med Imaging*. 2004;23:447–458.

25. Shorten C, Khoshgoftaar TM. A survey on image data augmentation for deep learning. *J Big Data*. 2019;6:1–48.

26. Parhi R, Nowak RD. The role of neural network activation functions. *IEEE Signal Processing Letters*. 2020;27:1779–1783.

27. Nurzynska K. Deep learning as a tool for automatic segmentation of corneal endothelium images. *Symmetry*. 2018;10:60.

28. Fabijańska A. *Corneal endothelium image segmentation using feedforward neural network*. in *2017 Federated Conference on Computer Science and Information Systems (FedCSIS)*. IEEE. 2017:629–637. ed.

29. Kolluru C, Benetz BA, Joseph N, Menegay HJ, Lass JH, Wilson D. Machine learning for segmenting cells in corneal endothelium images. In: *Medical Imaging 2019: Computer-Aided Diagnosis*. International Society for Optics and Photonics. 2019;10950:109504G.